

# A Numerical Study on Flow Control around Circular Disk using Coaxial Type DBD Plasma Actuator at Low Reynolds Number

H. Aono\*, S. Honami\* and H. Ishikawa\*  
Corresponding author: aono@rs.tus.ac.jp

\* Tokyo University of Science, JAPAN

**Abstract:** This paper numerically investigates the effects of flow control around a circular disk using the coaxial type dielectric barrier discharge plasma actuator (DBD-PA) and the drag force acting on the disk at the Reynolds number of 5,000. The disk is placed normal to the freestream direction. Two diameters of the coaxial type DBD-PA and several momentum coefficients are analyzed. The coaxial type DBD-PA body-force model is constructed based on the simple DBD-PA body-force distribution. Results demonstrate that the reduction of drag coefficient is obtained for all the cases considered in this study and the maximum reduction is 2.3%. It is found that the control effects on the surface pressure have tradeoff depending on the relative diameter of the coaxial type DBD-PA to the diameter to the disk. The large relative diameter of the coaxial type DBD-PA is the favorable effect on the control in terms of the time-averaged drag coefficient and the drag fluctuation.

*Keywords:* Flow Control, Plasma Actuator, Computational Fluid Dynamics, Low Reynolds Number, Circular Disk.

## 1 Introduction

Flow control using dielectric barrier discharge plasma actuators (DBD-PA) has been studied for improving the performance of many kinds of fluid machinery [1,2]. Figures 1 (a) and (b) show the schematic of common DBD-PA that consists of two electrodes and a dielectric material. When a high alternating current voltage is applied between two electrodes, non-thermal atmospheric plasma is produced, and this induces the plasma jet along the surface. The advantages of DBD-PA [1,2] are easy installation due to simple structure and good response, etc.

Recently, Toyozumi et al. have presented a “Flow Morphing” concept [3] that is the flowfield around the circular disk changed by using a coaxial type DBD-PA (see Figure 1 (c)) like the shape morphing technology [4]. By the force measurement and flow visualization, they have reported about 10% drag reduction in comparison with that without the coaxial type DBD-PA at the Reynolds number of 5,000 and different induced flow structures on the suction side of the disk due to the change of the diameter of the coaxial type DBD-PA. However, the drag reduction mechanisms have been inadequately discussed and remained unclear. Thus, current study aims to clarifying the drag reduction mechanisms associated with the coaxial type DBD-PA at low Reynolds numbers based on numerical simulations.

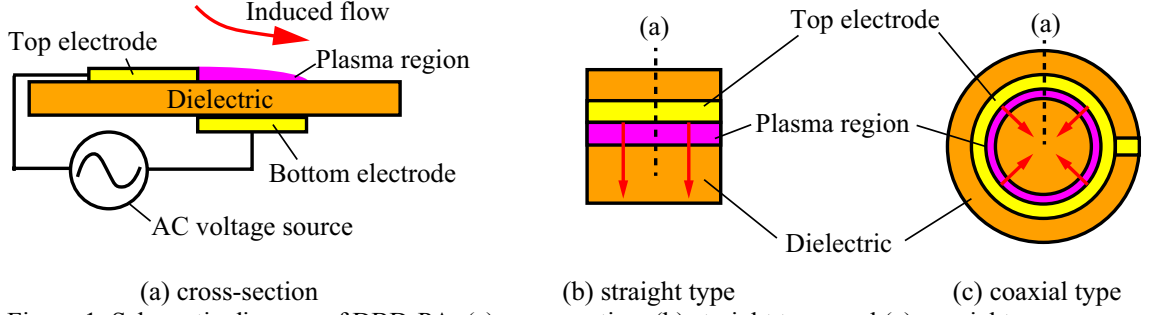


Figure 1: Schematic diagram of DBD-PA: (a) cross-section, (b) straight type, and (c) coaxial type

## 2 Problem Settings

### 2.1 Flow Conditions and Object Shape

The circular disk is selected as a typical, simple shape of a morphing object. The diameter of the circular disk  $D$  is set to 50mm as the reference length. The thickness of the circular disk  $t_d$  is 5mm. The thickness ratio  $t_d/D$  is 0.1. The disk has a shape edge. The freestream velocity  $U_\infty$  is set at 1.51m/s as the reference velocity. The Reynolds number  $Re$  is set to 5,000. The disk is placed normal to the freestream direction. The freestream Mach number  $Ma$  is set to 0.2 for all computations. This value is sufficiently small that compressibility of fluid is nearly negligible. Therefore, the flow field obtained by the simulations is considered to be similar to that with a lower freestream velocity. The specific heat ratio  $\gamma$  and Prandtl number  $Pr$  are set at 1.4 and 0.72, respectively.

### 2.2 Governing Equations

The governing equations are the three-dimensional compressible Navier-Stokes (NS) equations with the DBD-PA body-force term, normalized by the freestream density, the freestream velocity, and the diameter of the disk. The governing equations in the nondimensional form are written as follows:

$$\frac{\partial \rho}{\partial t} + \frac{\partial \rho u_j}{\partial x_j} = 0, \quad (1)$$

$$\frac{\partial \rho u_i}{\partial t} + \frac{\partial (\rho u_i u_j + p \delta_{ij})}{\partial x_j} = \frac{1}{Re} \frac{\partial \tau_{ij}}{\partial x_j} + D_c S_i, \quad (2)$$

$$\frac{\partial e}{\partial t} + \frac{\partial ((e+p)u_j)}{\partial x_j} = \frac{1}{Re} \left( \frac{\partial u_i \tau_{ij}}{\partial x_j} + \frac{1}{(\gamma-1)PrMa^2} \frac{\partial q_j}{\partial x_j} \right) + D_c S_j u_j, \quad (3)$$

$$S_i = Q_c E_i, \quad (4)$$

where  $x_i$ ,  $u_i$ ,  $q_i$ ,  $\rho$ ,  $p$ ,  $e$ ,  $\tau_{ij}$ ,  $\delta_{ij}$ ,  $S_i$ ,  $Q_c$ ,  $E_i$ , and  $t$  denote the nondimensional forms of the positional vector, velocity vector, heat flux vector, density, static pressure, total energy per unit volume, stress tensor, Kronecker delta, body-force vector, electric charge, electric-field vector, and time, respectively. The Reynolds number  $Re$ , Prandtl number  $Pr$ , and Mach number  $Ma$  are defined as follows:

$$Re = \frac{\rho_\infty U_\infty D}{\mu_\infty}, Pr = \frac{\mu_\infty C_p}{\kappa_\infty}, Ma = \frac{U_\infty}{a_\infty}, \quad (5)$$

where  $\mu_\infty$ ,  $U_\infty$ ,  $a_\infty$ ,  $C_p$ , and  $\kappa_\infty$  represent viscosity, velocity, speed of sound, constant-pressure specific heat, and thermal conductivity, respectively. The subscript  $\infty$  denotes the quantity under the freestream conditions. Here, the viscosity is computed using Sutherland's law. The last terms of the right-hand side in Eqs. (2) and (3) represent the momentum and the power added to the unit volume by the DBD-PA body-force model, respectively. The body-force terms are explained in the next subsection.

### 2.3 Coaxial Type DBD Plasma Actuator Body Force Model

The spatial distribution of the coaxial type DBD-PA body force model is constructed based on the Suzen-Huang plasma model [5] in this study. The spatial distribution of electrohydrodynamic body-force vectors in a plane are gained by solving two-partial differential equation of the Suzen-Huang plasma model [5] with a steady boundary condition representing the maximum forcing in advance. Then, the resultant body-force vectors in a plane distribute with a rotation of 360 degrees about the center of the disk (see Fig. 2). In the flow-control simulations, these electro-hydrodynamic body-force vectors into the right-hand side of the NS equations as the body-force terms, with the assumption that the magnitude of the distributed body force is proportional to the boundary condition. Furthermore, the nondimensional parameter  $D_c$  is defined as

$$D_c = \frac{Q_{c,ref} E_{ref} D}{\rho_\infty U_\infty^2}, \quad (6)$$

where  $Q_c$  and  $E_i$  denote the electric charge and the electric-field vector, and the subscript ref the reference value. The maximum values of  $Q_c$  and  $E$  in the pre-computation results of the Suzen-Huang model [5] used as  $Q_{c,ref}$  and  $E_{ref}$ .

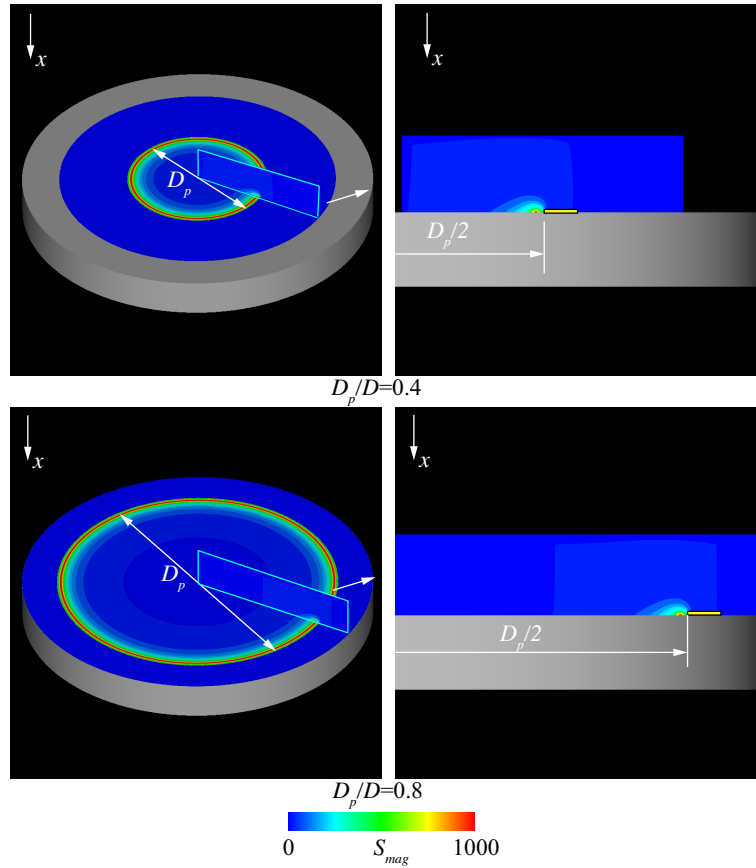


Figure 2: Spatial distribution of the coaxial type DBD-PA body force model. Note the yellow boxes in images of the right-hand side indicate the exposed electrode of the DBD-PA for the visualization purpose that is not physically existed in the computational model.

### 2.4 Operating Conditions of Body Force

The temporal-varying body forces are given as follows:

$$S(x, y, z, t) = S_{coaxial}(x, y, z) \sin^2(2\pi F_{base}^+ t) \quad (7)$$

where  $F_{base}^+$  is the nondimensional base frequency for the alternating current of the input voltage, and  $S_{coaxial}(x, y, z)$  is the body-force vectors of the coaxial type DBD PA body-force model that are explained in previous subsection. The nondimensional frequency  $F_{base}^+$  of the sinusoidal base wave is set to 200, which is higher for flow fluctuation. As stated in Eq. (7), a square of the sinusoidal function is chosen as the temporal change of body-force because the time-varying force generated by the DBD-PA might be described as a push-push type in one cycle, which is similar to the square of the sinusoidal function [6]. The parameter  $D_c$  could be linked with the momentum coefficient  $c_\mu$ , which is defined as follows:

$$c_\mu = \frac{D_c \iiint S_{mag} dx dy dz}{\sqrt{2} \cdot 0.5 \rho_\infty U_\infty^2 D}, \quad (8)$$

where  $S_{mag} = \sqrt{S_x^2 + S_y^2 + S_z^2}$ . Note the body force is averaged out in the period of  $1tU_\infty/D$ .

## 2.5 Effects of $D_c$ and $D_p$ on Maximum Induced Jet Velocity in Quiescent Air

In current approach, a priori fluid-dynamic simulations in the quiescent air are required to set the value of  $D_c$  for flow-control simulations. Moreover, the change of diameter of the coaxial type DBD-PA also leads to the change of  $c_\mu$ . Thus, simulations of each  $D_p$  with  $D_c=0.025, 0.050, 0.100,$  and  $0.200$  in the quiescent air are carried out in order to check the maximum average induced jet velocity. As a result, it is found for the  $D_p/D=0.4$  cases approximately 24.4%, 37.7%, 57.4%, and 86.8% of the freestream velocity (i.e. 0.370, 0.569, 0.867, and 1.31 m/s) in the  $D_c=0.025, 0.050, 0.100,$  and  $0.200$  cases, and for the  $D_p/D=0.8$  cases about 18.6%, 29.3%, 46.6%, and 73.8% of the freestream velocity (i.e. 0.281, 0.443, 0.704, and 1.11 m/s) in the  $D_c=0.025, 0.050, 0.100,$  and  $0.200$  cases, respectively. From this assessment, the  $D_c$  are set to less than 0.100 for the flow-control simulations performed in this study. Note that the computed average maximum plasma jet velocities in the quiescent air are less than 1 m/sec that are within the realistic range and measurements reported in the previous study [3].

## 2.6 Case Setup

The operational conditions of the coaxial type DBD-PA in this study are shown in Table 1. The coaxial type DBD-PA continuously switches on. To investigate the effects of the diameter of coaxial type DBD-PA and the momentum coefficient  $c_\mu$  on control performance and mechanisms, the ratio of  $D_p$  and  $D$  are set to 0.4 and 0.8, and the momentum coefficients  $c_\mu$  varies from  $1.082 \times 10^{-2}$  to  $9.454 \times 10^{-2}$ , respectively.

Table 1: List of computational case and the maximum induced jet velocity in the quiescent air

| Case name    | $D_p/D$ | $D_c$ | $c_\mu$                | $u_{i,max}/U_\infty$ |
|--------------|---------|-------|------------------------|----------------------|
| No control   | -       | -     | -                      | -                    |
| Dp0.4Dc0.025 | 0.4     | 0.025 | $1.082 \times 10^{-2}$ | 0.244                |
| Dp0.4Dc0.050 | 0.4     | 0.050 | $2.164 \times 10^{-2}$ | 0.377                |
| Dp0.4Dc0.100 | 0.4     | 0.100 | $4.327 \times 10^{-2}$ | 0.574                |
| Dp0.8Dc0.025 | 0.8     | 0.025 | $2.364 \times 10^{-2}$ | 0.186                |
| Dp0.8Dc0.050 | 0.8     | 0.050 | $4.727 \times 10^{-2}$ | 0.293                |
| Dp0.8Dc0.100 | 0.8     | 0.100 | $9.454 \times 10^{-2}$ | 0.466                |

# 3 Computational Approach

## 3.1 Numerical Method

The three-dimensional compressible NS equations with DBD-PA body-force terms are employed as the governing equations. Those equations are numerically solved in the generalized curvilinear coordinates  $(\xi, \eta, \zeta)$ . The spatial derivatives of convective term are evaluated by SHUS [7] with third-

order MUSCL [8] scheme and of viscous term are evaluated by second-order central difference scheme. For time integration, the second-order backward difference is employed and it is converged by the three sub-iterations [9] of the alternating directional implicit symmetric Gauss-Seidel implicit method [10] in each time step. Any sub-grid scale and turbulence models are not adopted. The non-dimensional computational time step is  $2.5 \times 10^{-3} D/U_\infty$  that corresponds to the maximum local Courant number becomes approximately 2. At the outer boundaries, all variables are extrapolated from one point inside of the boundary. At the inlet boundary, the freestream velocity is assigned without any fluctuation. A no-slip and adiabatic boundary condition is adopted for the surface of the circular disk. For the singular points, flow variables are replaced by the average of surrounding nodes.

### 3.2 Computational Grids

A zonal method [11] is used to deal with the small velocity induced by the coaxial DBD-PA and flow around the circular disk. Figure 3 shows the computational grids around the circular disk and compose of four individual zones. An O-type topology is adopted for the plane normal to the freestream. The first grid points away from the circular disk surface are  $3.5 \times 10^{-4} D$ . The outer boundary normal and parallel to freestream is set at about  $50D$  and  $125D$  away from the circular disk in order to minimize the influence of outer boundaries on the flow near the disk. Number of computational grid points for each case is summarized in Table 2.

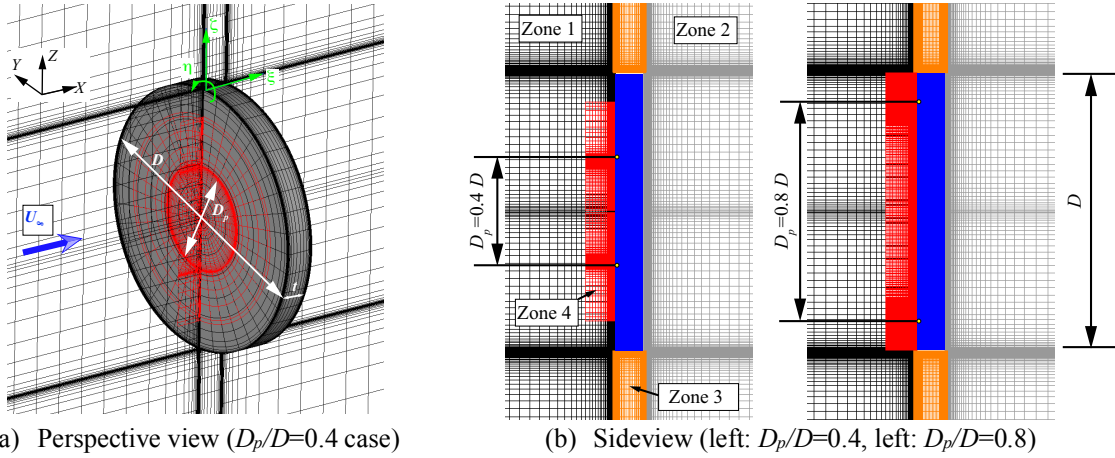


Figure 3: Computational grid around the disk (a) and computational grid distribution (b) in the section (the  $\xi$ - $\zeta$  plane or the  $\xi$ - $\eta$  plane). Black, grey, orange, and red colored grids denote Zone 1, Zone 2, Zone 3, and Zone 4, respectively.

Table 2: Number of computational grid point for each case.

|                              | Grid of $D_p/D=0.4$ ( $\xi \times \eta \times \zeta$ ) | Grid of $D_p/D=0.8$ ( $\xi \times \eta \times \zeta$ ) |
|------------------------------|--|--|
| Zone 1 (upstream region)     | 93×121×140   | 87×121×114   |
| Zone 2 (downstream region)   | 221×121×140  | 197×121×134  |
| Zone 3 (side of disk region) | 77×121×97  | 77×121×91  |
| Zone 4 (DBD-PA region)       | 42×121×89  | 42×121×223   |

### 3.3 Verification and Validation of Computed Results

Verification and validation of the simulated results in the case without control are discussed here. For the verification study, a grid sensitivity analysis based on three different grids of the disk for the  $D_p/D=0.2$  case, a coarse grid (Grid 1) with 4.37 million grids, a medium grid (Grid 2) with 5.38 million grids, and a fine grid (Grid 3) with 6.68 million points, is carried out. The number of grid points in each dimension is presented in Table 3.

The time-averaged drag coefficient  $C_D$  of Grid 1, Grid 2, and Grid 3 are 1.1845, 1.1878, and 1.1934, respectively, and the difference among them is less than 0.746%. In addition, Fig.4 shows comparisons of the time and azimuth averaged surface pressure coefficient  $C_p$  along the disk from the center of the suction side to the edge and from the edge to the center of the pressure side. In Fig.4,  $l$  is defined as a distance from the center of the suction side of the disk surface. The  $C_p$  distributions on the suction side are almost the same. While the  $C_p$  distributions on the pressure side show slight difference and the difference between the results of Grid 2 and Grid 3 is sufficiently small.

Table 3: Number of grid point for grid sensitivity assessment.

|                              | Grid 1 ( $\xi \times \eta \times \zeta$ ) | Grid 2 ( $\xi \times \eta \times \zeta$ ) | Grid 3 ( $\xi \times \eta \times \zeta$ ) |
|------------------------------|---|---|---|
| Zone 1 (upstream region)     | $60 \times 121 \times 104$                | $78 \times 121 \times 122$                | $93 \times 121 \times 140$                |
| Zone 2 (downstream region)   | $188 \times 121 \times 104$               | $206 \times 121 \times 122$               | $221 \times 121 \times 140$               |
| Zone 3 (side of disk region) | $77 \times 121 \times 61$                 | $77 \times 121 \times 79$                 | $77 \times 121 \times 97$                 |

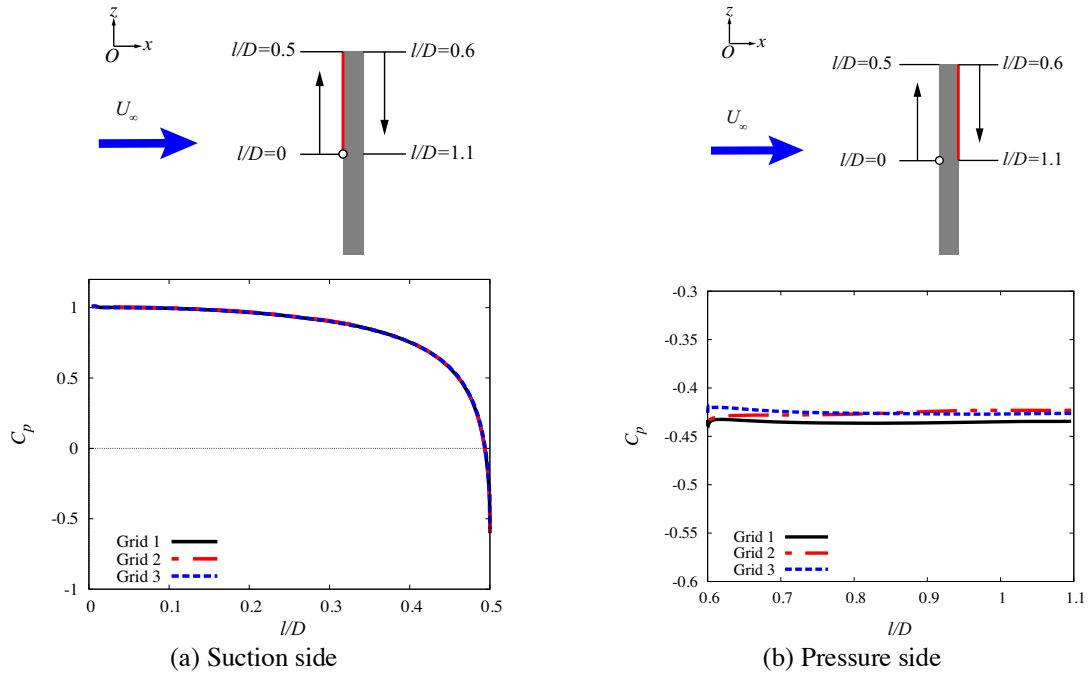


Figure 4: Comparisons of the distributions of time and azimuth averaged surface pressure coefficient  $C_p$  among three grids.

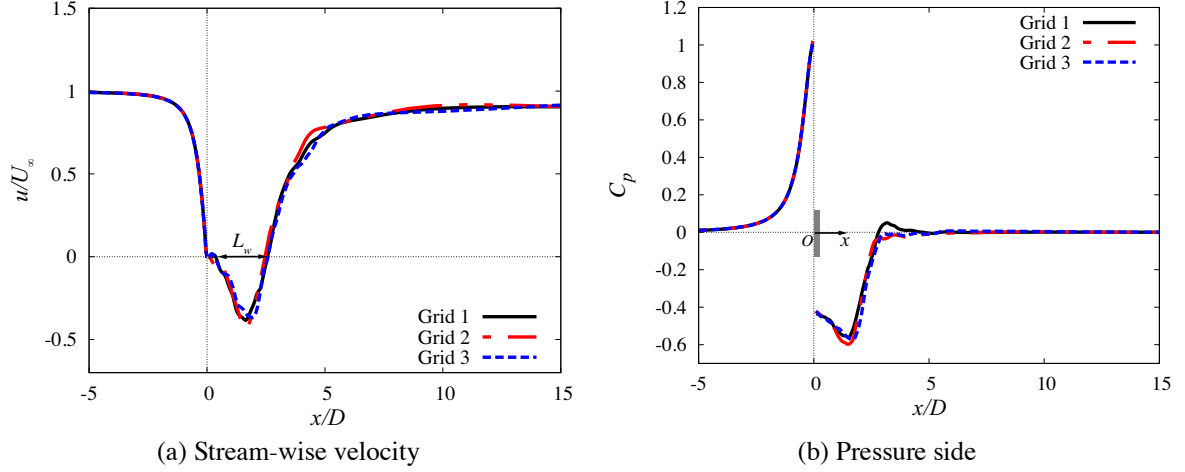


Figure 5: Comparisons of the distributions of time-averaged (a) stream-wise velocity  $u/U_\infty$  and (b) pressure coefficient  $C_p$  along the centerline of the disk among three grids.

Figure 5 presents comparisons of the distribution of the time-averaged streamwise velocity  $u/U_\infty$  and pressure coefficient  $C_p$  along the centerline of the disk. In Fig. 5,  $L_w$  represents the mean recirculation length.  $L_w$  and  $C_p$  distribution has slight difference among three grids but the difference is small enough. According to results presented here, the fine grid (Grid 3) is used for all computations of the  $D_p/D=0.4$  case. Note that we think that the grid resolution used in this study has sufficiently resolved the turbulent flow in the wake region to discuss the control effects for all the cases.

Table 4: Comparisons of time-averaged  $C_D$ ,  $Re$ , and  $td/D$  for the validation study of the case without control.

|        | Current study   | Ref. [3]        | Ref. [12]        | Ref. [13]        | Ref. [14]        | Ref. [15]        |
|--------|-----------------|-----------------|------------------|------------------|------------------|------------------|
| $C_D$  | 1.1934          | 1.3             | 1.17             | 1.096            | 1.34-1.35        | 1.4              |
| $Re$   | $5 \times 10^3$ | $5 \times 10^3$ | $10 \times 10^3$ | $33 \times 10^3$ | $33 \times 10^3$ | $10 \times 10^3$ |
| $td/D$ | 0.1             | 0.1             | 0.0              | 0.015            | 0.3-0.5          | 0.062            |

For the validation of the case without control, the time-averaged drag coefficient  $C_D$  is compared with the available experimental data. Table 4 shows comparisons of the time-averaged  $C_D$ . The computed time-averaged  $C_D$  is smaller than that reported in Toyozumi et al. [3]. The reason of this discrepancy most likely comes from the blockage effects in the wind tunnel [3] and the difference in inlet flow condition between the computation and the experiment. Moreover, it is found that other relevant studies have reported relatively large variation in the time-averaged  $C_D$  (its range are between 1.096 and 1.4) due to the blockage effects in the wind tunnel and the flow condition at the inlet and so on. Considering the uncertainty of the experimental data, difficulties in measuring small force acting the disk under low freestream conditions, and grid resolution used current numerical simulations, we think that the computed  $C_D$  in this study is acceptably reliable. Quantitative comparison between the experiment and the computation such as the surface pressure distribution should be conducted in near the future. Note that the fluid dynamic solver used in this study has been validated for airfoil-flow control simulations at the Reynolds number of  $O(10^4-10^5)$  [16, 17].

### 3.4 Computational Sequence and Processed Data

At first, the computation impulsively starts without the coaxial type DBD-PA. The computation keeps running until initial transient influences are completely faded ( $60tU_\infty/D$ ). Then, the flow around the disk at time instant of  $60tU_\infty/D$  is used as the initial condition for all flow-control simulations with the coaxial type DBD-PA. Figure 6 plots time histories of  $C_D$  and indicates the time duration for the averaging. The computation is conducted until  $110tU_\infty/D$  for the no-control case and  $50tU_\infty/D$  for all

control cases.

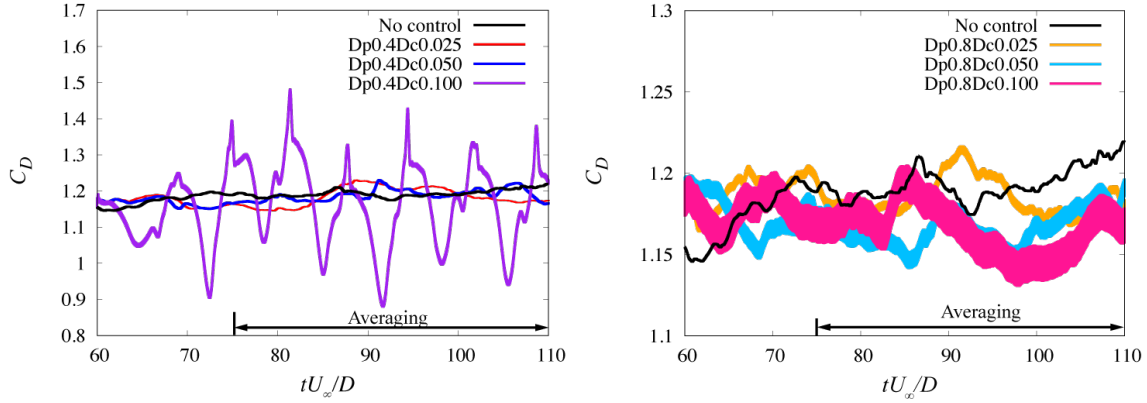


Figure 6: Time histories of drag coefficients  $C_D$ . Left plot includes  $D_p/D=0.4$  and right  $D_p/D=0.8$  cases, respectively. The case without the control denotes “No control” in the figure caption.

## 4 Results and Discussions

### 4.1 Discussion on Averaged Data

#### 4.1.1 Aerodynamic Performance

Figures 6 and 7 show the time histories of the drag coefficient  $C_D$  and the time-averaged  $C_D$  for each case. In Fig. 7, the error bars represent the standard deviation of  $C_D$  for the averaged duration. Owing to the flow control, the time-averaged  $C_D$  decreases in all the cases with the control. The variations in the  $D_p/D$  and  $D_c$  or  $c_\mu$  considerably affect drag reduction. Maximum time-averaged  $C_D$  reduction in comparison with the case without the control (no control) is 2.3%. For the cases with  $D_c=0.025$  the drag reduction is very small.

For the  $D_p/D = 0.4$  with  $D_c=0.100$  case, the averaged  $C_D$  is remarkably reduced but has large standard deviation. Indeed, time history of  $C_D$  shown in Fig. 6 clearly presents that the waveform of the  $D_p/D = 0.4$  with  $D_c=0.100$  case is highly different from other cases and  $C_D$  fluctuates with the large amplitude and low frequency. While for the  $D_p/D = 0.8$  case, the averaged  $C_D$  decreases without the unfavorable flow behavior that is found in the  $D_p/D = 0.4$  case. Time histories of  $C_D$  in the  $D_p/D = 0.8$  with  $D_c=0.050$  and  $0.100$  cases show similar waveform and shift down. Furthermore, the control performance of the smaller diameter of the coaxial type DBD-PA is more sensitive to the change of  $D_c$  or  $c_\mu$  and the standard deviation of the time-averaged  $C_D$  in comparison with that of no control case is increased in the cases of the  $D_p/D = 0.4$ . This is mainly due to the difference in the flow structures around the disk

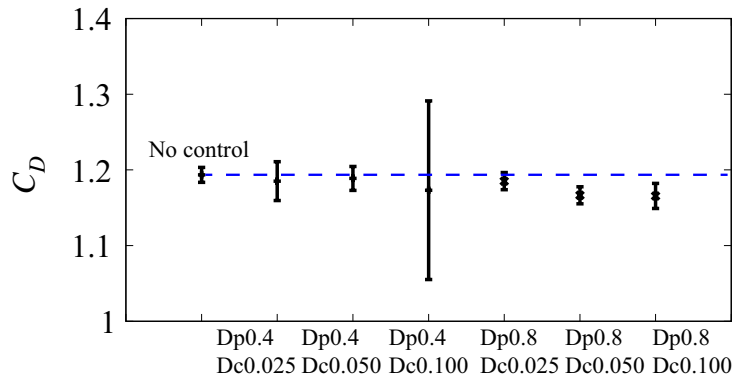


Figure 7: Time-averaged drag coefficients  $C_D$ . Dashed line indicates the averaged  $C_D$  in the case without control. The error bars represent the standard deviation of  $C_D$ .

#### 4. 1. 2 Stream-wise Velocities, Turbulent Kinetic Energy, and Surface Pressure

Figure 8 shows streamlines, the time-averaged stream-wise velocity  $u/U_\infty$ , and turbulent kinetic energy (TKE) distribution around the disk in the  $x$ - $z$  plane. Here, the TKE is defined as  $(u'^2 + v'^2 + w'^2)/(2U_\infty^2)$ .

For all the control cases, vortex-like flow structures are observed on the suction side. The interaction between the induced jet and freestream leads to such interesting flow structures on the suction side. Those flow structures have been also seen from the experimental flow visualization [3]. For the  $D_p/D=0.4$  cases the vortex-like flow structures are more clearly identified and size of the vortex increases with the increase of  $D_c$  or  $c_\mu$ . Increasing the size of the vortex produces large reversed flow region and high TKE region. This observation suggests that the vortex-like flow structure is not steady in the time. While the  $D_p/D=0.8$  cases very low magnitude of TKE region on the suction side is seen. This implicates that the vortex-like flow structure seems to be steady in the time unlike the  $D_p/D=0.4$  with  $D_c = 0.050$  and  $0.100$  cases. This will be discussed in next subsection based on the instantaneous flow structures.

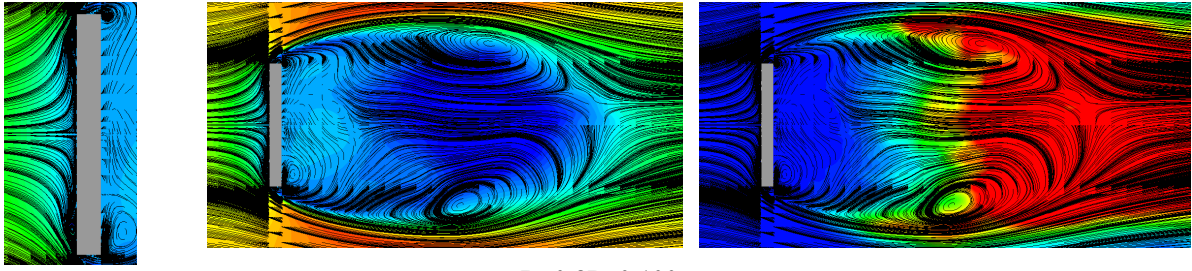
In the wake flow structure, fundamental flow structures are similar for all the cases. However, the location of roll-up of the separated shear layer shows difference due to the control. For the  $D_p/D=0.4$  cases, the location of roll-up of the separated shear layer moves closer to the disk while for the  $D_p/D=0.8$  cases the location moves to the downstream. If the results of the  $D_p/D=0.4$  and  $0.8$  with  $D_c=0.100$  cases are compared, the difference of the location is clearly observed. This difference in the wake flow affects the surface pressure  $C_p$  on the pressure side of the disk and drag force generation.

Figure 9 plots the surface pressure  $C_p$  distribution on the suction side and the pressure side of the disk. For the suction side of the disk, the pressure near the edge of the exposed electrode of the DBD-PA significantly decreases. For the  $D_p/D=0.4$  case, the pressure on  $l/D=0.2$  to  $0.45$  decreases due to the coaxial type DBD-PA. This pressure reduction of the suction side of the disk also works positively regarding the drag reduction. For the  $D_p/D=0.8$  case, the pressure around the exposed electrode of the coaxial type DBD-PA increase that works negatively for drag reduction. On the other hand, the effects of the control on the pressure distribution on the pressure side of the disk present completely opposite way (i.e. the pressure decreases for the  $D_p/D=0.4$  cases while the pressure increases for the  $D_p/D=0.8$  cases.) In terms of suppressing drag generation, the reduction of the surface pressure on the pressure side is good. This suggests that the  $D_p/D=0.8$  cases have favorable control effects on the pressure side.

Figure 10 shows comparisons of the distributions of time and azimuth averaged streamwise velocity and pressure coefficient along the centerline of the disk. It is observed that for the  $D_p/D=0.4$  with  $D_c=0.100$  case, the location of minimum stream-wise velocity and pressure coefficient is the closest to the disk in all the case and for the  $D_p/D=0.4$  cases the starting location of the recirculation region is the most far from the disk. Those difference in the distribution of the streamwise velocity and pressure coefficient are linked with the performance of drag reduction.

Summing up, there is a tradeoff for the effects of the control using the coaxial type DBD-PA on between the pressure distribution on the suction side and the pressure side of the disk. For the  $D_p/D=0.4$  case, the strong and large size of vortex-like flow structures are generated by the interaction between freestream and the induced jet and those produce low pressure region on the suction side. Those vortex structures collapse and convect to downstream. Those disturb the separated shear layers from the leading-edge of the disk. On the other hand, for the  $D_p/D=0.8$  with  $D_c=0.050$  and  $0.100$  cases the small size of the vortex-like flow structures are produced on the suction side of the disk and this vortex structure maintain the three-dimensional, stable ring-like shape. This seems to change separated shear layer and delay the roll-up motion of the separated shear layer from the leading-edge.





Dp0.8Dc0.100

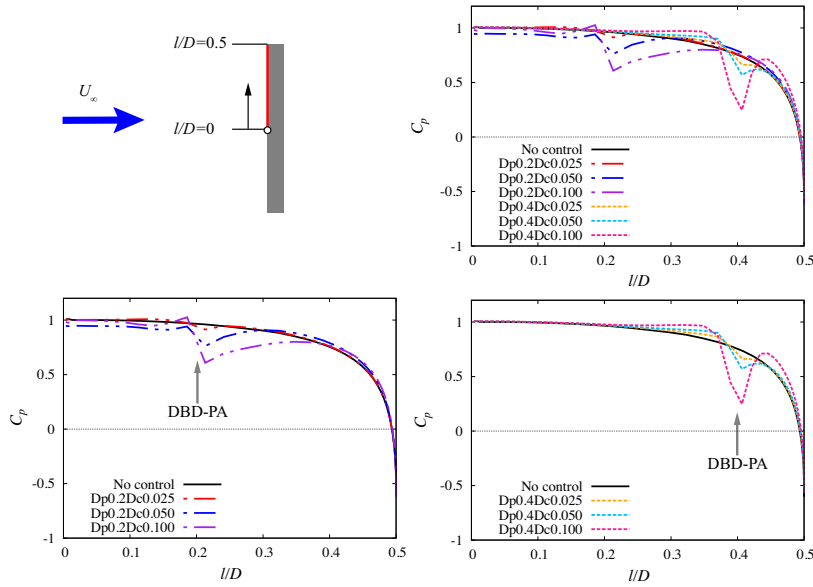
-0.05  $u/U_\infty$  0.25

0 TKE 0.001

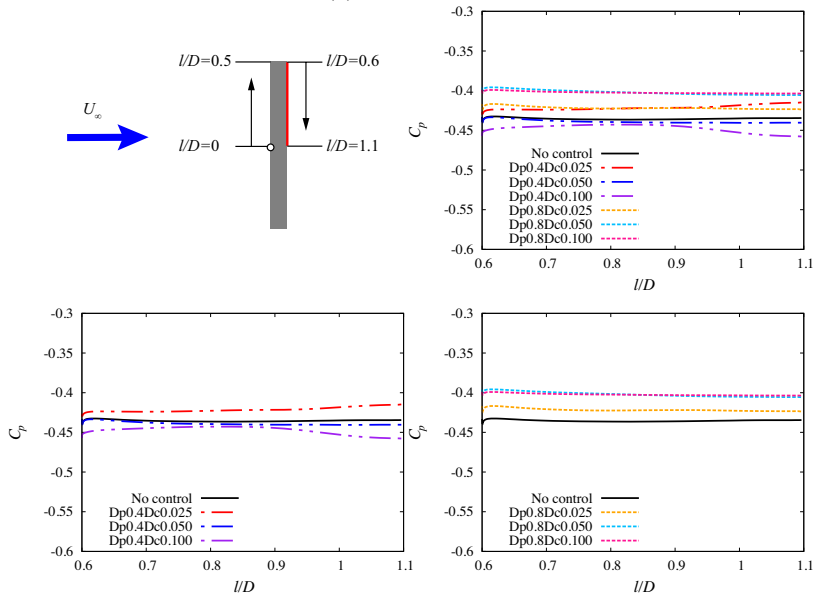
Near the disk

Wake

Figure 8: Comparison of distribution of time-averaged stream-wise velocity  $u/U_\infty$  and turbulent kinetic energy TKE around the disk at the  $x$ - $z$  plane ( $y=0$ ).

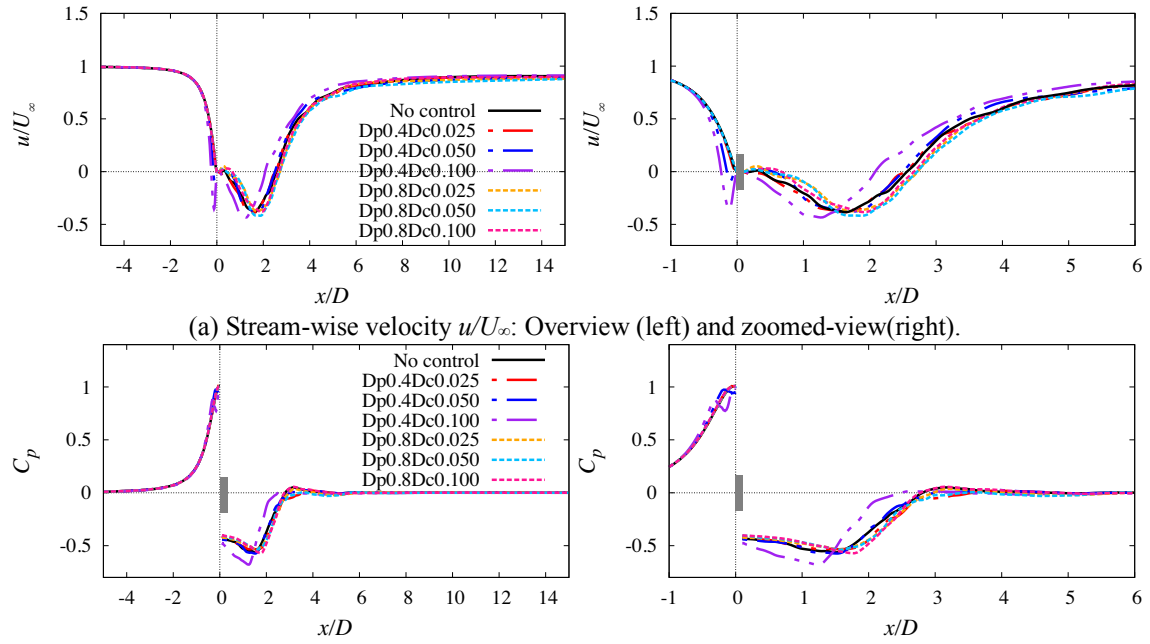


(a) Suction side



(b) Pressure side

Figure 9: Comparisons of distribution of time and azimuth averaged surface pressure coefficient  $C_p$  of the disk.



(a) Stream-wise velocity  $u/U_\infty$ : Overview (left) and zoomed-view(right).

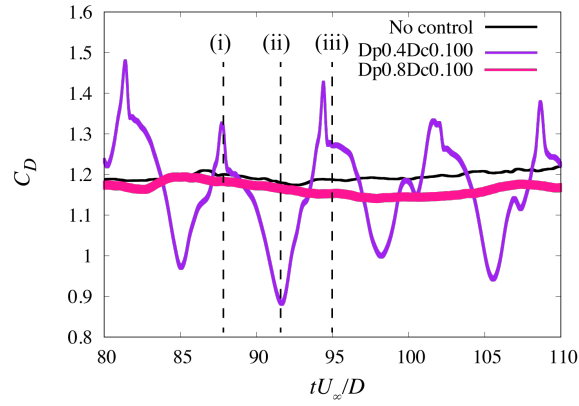
(b) Pressure coefficient  $C_p$ : Overview (left) and zoomed-view(right).

Figure 10: Comparisons of the distributions of time and azimuth averaged streamwise velocity (a) and pressure coefficient along the centerline of the disk.

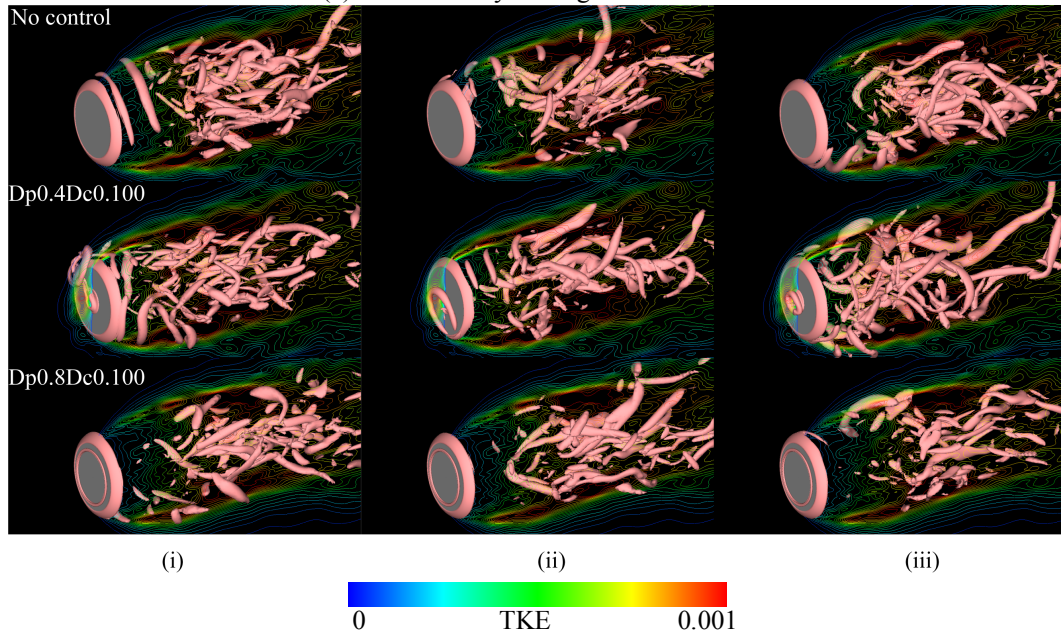
## 4.2 Discussion on Unsteady Data

Figure 11 shows time histories of  $C_D$  for time period between  $80tU_\infty/D$  to  $110tU_\infty/D$  and instantaneous flow structures around the disk at selected time instants. The iso-surfaces represent the second invariant of velocity gradient tensor ( $Q$ -criterion) [18] and the color contour indicates the TKE distribution in the  $x$ - $z$  plane around the disk.

For the  $D_p/D=0.4$  with  $D_c=0.100$  case (Dp0.4Dc0.100), at time instants of (i), (ii), and (iii)  $C_D$  reaches either very low or very high and the vortex-like flow structure observed on the suction side of the disk collapses. While the  $D_p/D=0.8$  with  $D_c=0.100$  case (Dp0.8Dc0.100), the vortex-like flow structure is maintained on the suction side of the disk. In the wake region, three-dimensional turbulent vortices can be seen for all the cases. In comparison with those of the case without control, for the  $D_p/D=0.4$  with  $D_c=0.100$  case, three-dimensional vortical structures are presented near the disk while the  $D_p/D=0.8$  with  $D_c=0.100$  case those show far from the disk and less number of turbulent vortices.



(a) Time history of drag coefficient  $C_D$



(b) Instantaneous flow structures: iso-surface is  $Q$ -criterion ( $Q=1$ ) and the color contour is turbulent kinetic energy TKE in the plane

Figure 11: Time history of drag coefficients and instantaneous flow structures around the disk at selected time instants.

## 5 Concluding Remarks

This paper has numerically investigated the effects of the coaxial type DBD-PA on the flow around the 10% thickness circular disk and the drag force acting on the disk. The Reynolds number is set to 5,000. The disk is placed normal to the freestream direction. Two diameters of the coaxial type DBD-PA are considered (i.e.  $D_p/D=0.4$  and 0.8 cases). Results of aerodynamic data have presented that drag coefficient  $C_D$  decreases due to the flow control by the coaxial type DBD-PA and maximum reduction of  $C_D$  is approximately 2.3%. The  $D_p/D=0.8$  case shows lower fluctuation and similar drag reduction of the  $D_p/D=0.4$  case with almost the same momentum coefficient  $c_{\mu}$ .

It is revealed that interesting flow dynamic phenomena are responsible for the drag reduction of the circular disk normal to the air-stream due to flow control using the co-axial DBD-PA. First one is the low-pressure region produced by the interaction between the induced jet and freestream on the suction side of the disk and second is the delayed roll-up motion of the separated shear layer from the edge of the disk. The relative diameter of the coaxial type DBD-PA to the disk is an important parameter for determining the dominant flow dynamic phenomena. From the results of current study, the large relative diameter of the coaxial type DBD-PA (i.e.  $D_p/D=0.8$  case) is the favorable effect on control in terms of the time-averaged drag coefficient and the drag fluctuation. The drag reduction performance and effectiveness of flow control by the coaxial type DBD-PA for the higher freestream

velocity conditions are left for future work.

## Acknowledgements

This work was partially supported by JSPS KAKENHI Grant Number JP17K06168.

## References

- [1] E. Moreau. Airflow control by non-thermal plasma actuators, *J. Phys. D.* 40: 605-636, 2007.
- [2] L. N. III. Cattefesta, M. Sheplak. Actuator for active flow control, *Annu. Rev. Fluid Mech.* 43: 247-272, 2011.
- [3] S. Toyozumi, et al. Flow morphing by coaxial type plasma actuator, *Proc. 15<sup>th</sup> ACFM15*, USB2016.
- [4] S. Barbarino, et al. A review of morphing aircraft, *J. Intell. Material Syst.* 22: 823-877, 2011.
- [5] Y. B. Suzen, et al. Numerical simulation of plasma based on flow control application, *AIAA paper 2005-4633*.
- [6] G. I. Font, et al. Plasma volumetric effects on the force production of a plasma actuator. *AIAA J.* 48: 1869-1887, 2010.
- [7] E. Shima and T. Jonouchi. Role of CFD in aeronautical engineering. No. 14: AUSM type upwind schemes, Special publication of national aerospace laboratory, 7-12, 1997.
- [8] B. van Leer. Towards the ultimate conservation difference scheme. IV: a new approach to numerical convection. *J. Comp. Phys.* 23: 276-299, 1977.
- [9] S. R. Chakravarthy. Relaxation methods for unfactored implicit upwind schemes. *AIAA paper 1984-0165*, 1984.
- [10] K. Fujii. Simple ideas for accuracy and efficiency improvement of the compressible flow simulation methods, *Proc. ICFD workshop of STD*, SP-069029E, 1998.
- [11] K. Fujii. Unified zonal method based on the fortified solution algorithm, *J. Comp. Phys.* 118: 92-108, 1995.
- [12] S. F. Hoerner. Fluid-dynamic drag, *Hoerner Fluid Dynamics*. 1965.
- [13] M. Knight. Wind tunnel standardization disk drag, *NACA-TN-253*, 1936.
- [14] T. Igarashi, et al. Drag reduction of a circular disk normal to air-stream applying turbulent transition, *JSME Bullen B* 72: 1727-1734, 2006 (in Japanese).
- [15] J.A. Roberson, et al. Turbulence effects on drag of sharp-edge bodies. *J. Hydraul Div* 98: 1187-1203, 1972.
- [16] M. Sato, et al. Mechanisms for laminar separated-flow control using dielectric-barrier-discharge plasma actuator at low Reynolds number, *Phys. Fluids* 27: 117101, 2015.
- [17] H. Aono, et al. Plasma-actuator burst-mode frequency effects on leading-edge flow-separation control at Reynolds number  $2.6 \times 10^5$ , *AIAA J.* 55: 3789-3806, 2017.
- [18] J. Jeong and F. Hussan. On the Identification of Vortex, *J. Fluids Mech.* 28: 69-94, 1995.